Journal of Inorganic and General Chemistry

ZAAC

Zeitschrift für anorganische und allgemeine Chemie

www.zaac.wiley-vch.de

RESEARCH ARTICLE

Check for updates

Direct Laser Synthesis of Fe_2O_3 Modified TiO_2

V. V. Lennikov,[a] A. Gómez-Herrero,[b] L. A. Angurel,[a] G. F. de la Fuente,*[a] and
L. C. Otero-Díaz[c]

Dedicated to Prof. Martin Jansen on the occasion of his 80th birthday

A very fast, selective CO_2 laser line scan direct synthesis method is presented and has been applied here to study phase and defect formation within an irradiated mixture of powdered oxides, as a proof-of-principle. A nominal composition interval of $0 < x < 0.03$ was conveniently chosen for the $TiO_2 + xFe_2O_3$ system herein reported. X-ray diffraction analyses were used to determine the main crystalline phase composition. Thus, for 3% mol. Fe_2O_3, pseudobrookite crystals were found to coexist with rutile-type $MO_{2-\delta}$ (M=Ti, Fe) with extended defects. These are composed mainly of $(121)_r$ and $(132)_r$ crystallographic shear planes (CSP's), where r subindex refers to the rutile subcell. For samples with a lower Fe_2O_3 content (2, 1, 0.5% mol) only iron-doped rutile phases were observed, with complex microstructure arising from the presence of multi-twinned $(011)_r$ and $(110)_r$ crystals and isolated and/or ordered CSP's at short length scale. The diverse microstructures observed in the CO_2 laser produced samples correlate with the conditions imposed during the laser treatment, which include intrinsically high solidification rates and steep temperature gradients.

Introduction

Interest in materials based on titanium dioxide has been increasing during the last several decades, because they are attractive candidates for a vast number of applications. These include, among others, catalysis and photocatalysis, energy storage and production, pigments, cosmetics, sensors and electronics.[1–5] The $Fe_xTi_{1-0,75x}O_{2-y}$ solid solution has been reported to exist in the range $0.01 < x < 0.14$,[6] although some authors suggest a narrower range of values.[7] The introduction of Fe into TiO_2 has been reported to favor rutile formation[3] and seems to be of interest because of modifying the latter's band gap towards lower energies. This provides advantages for applications based on solar irradiation processes, as well as for the development of ceramic pigments with attractive reddish color, as the band gap is displaced towards the visible part of the electromagnetic spectrum. However, in both of these cases there is a need to control the homogeneity and to obtain small,

submicron powders which may be evenly distributed within an appropriate solid matrix or glaze.[8]

The development of a new method of material synthesis – selective laser line scan synthesis – opens new possibilities to produce materials at high temperatures with controlled microstructure and functional properties within a very short time. In addition, it is scalable to large areas and continuous synthesis/ fabrication processes. Laser Line Scanning is based on a Laser Zone Melting method previously applied to directionally solidify ZrO_2 eutectics[9] and Bi-based metal oxide superconductors.[10–11] It was originally applied to achieve high critical current values in this type of superconductors, textured in planar geometry.[12] This simple synthesis method essentially entails heating or melting of the component powder mixtures with the corresponding stoichiometry to yield a specific, desired solid product. The powder mixture is placed inside a metal or ceramic crucible to be irradiated with a linearly-shaped laser beam.[13] The use of a CO_2 laser emitting at $\lambda = 10,6$ μm opens the possibility to heat essentially any oxide material, since optical absorption at this wavelength is efficient for most metal oxides. Medium power lasers are sufficient to reach melting temperatures well above 2500 °C. These may be combined with commercially available optical beam steering elements to enable achieving high definition laser energy profiles when heating any desired geometry sample. The Laser Line Scan process itself opens the possibility of processing under non-equilibrium conditions, providing also potentially new paths to the synthesis of unusual phases. These may be particularly induced by the large temperature gradients and fast cooling rates characteristic to the method, allowing to explore a limited part of the vast energy landscape of solids proposed by Jansen.[14,15]

Related studies have appeared long ago in the literature, reporting on Fe_2O_3-TiO_2 samples obtained by more conventional means. The latter included essentially solid state sintering

[a] V. V. Lennikov, L. A. Angurel, G. F. de la Fuente
INMA (CSIC – Universidad de Zaragoza), Mª de Luna, 3, Zaragoza, Spain
E-mail: german.delafuente.leis@csic.es
[b] A. Gómez-Herrero
ICTS Centro Nacional de Microscopía Electrónica, Universidad Complutense de Madrid, 28040 Madrid, Spain
[c] L. C. Otero-Díaz
Facultad de Ciencias Químicas, Dpto. de Química Inorgánica I, Universidad Complutense, Madrid, Spain

methods at temperatures within the 900–1500 °C range, carried out inside electrical furnaces during periods of days or weeks. The reported syntheses occasionally included annealing at temperatures below those used for sintering.[16–18] In addition, they also provided exhaustive electron diffraction studies on 0–25 mol% Fe_2O_3-TiO_2 samples, where crystallographic shear planes (CSPs) have been suggested to remain with essentially constant spacings, but to vary their orientations cooperatively when subjected to temperatures near the melting point of the solid mixture ($\geq$ 1550 °C).[19]

The main objective of this work was thus to assess the applicability of the selective Laser Line Scan method to the synthesis of selected TiO_2-Fe_2O_3 samples, in order to compare the products obtained with those reported in the literature. In this manner, microstructure and appearance of the products could be ascertained for potential applications as ceramic pigments. High resolution electron microscopy was used to characterize the possible incorporation of Fe oxide phases into TiO_2, as well as the defects induced by this laser processing method on the products obtained.

Experimental

Precursor Preparation

Titanium dioxide in the form of rutile (Aldrich, purity 99,95 %) and iron (III) oxide in the form of hematite (Aldrich, purity 99,95 %) both dried at 300 °C during 6 hours were used as starting materials for the syntheses of the selected compositions given in Table 1. Mixtures of TiO_2:Fe_2O_3 with molar ratios 1:0.005, 1:0.01, 1:0.02, 1:0.03 were prepared. The corresponding quantities of both metal oxides were mixed in acetone, milled using a Retch MM2000 apparatus containing agate milling media at a power level of 80 % during 10 min. Acetone was removed by heating at 150 °C during 3 hours.

Laser Line Scan synthesis

A Rofin-Sinar Model SC x30 SLAB-type CO_2 laser operating in pulsed mode was used to perform the Selective Laser Line Scan Synthesis experiments described in this work. The experimental apparatus is shown in Figure 1. A circular laser output beam with an average output power level of 200 W was focused, using a gold-plated parabolic mirror, into a long, thin line, measuring approx. 20 mm in length and 0.5 mm in width. The oval line appeared symmetrically shaped, with the largest width in its center.

The mixture of oxides was placed in a Nd:YAG surface-treated aluminum crucible. This ablated aluminum surface does not reflect incoming CO_2 laser ($\lambda = 10.6$ μm) radiation significantly, avoiding personnel and equipment safety problems. In addition, the high thermal conductivity of the crucible helps to maintain it at a sufficiently low temperature to avoid excessive heating and undesired reactivity with the melting powder mixture. The crucible was moved in one axis (horizontal), perpendicular to the focused laser line, at a speed of 50 mm/min, in order to melt powders at temperatures approaching 2000 °C with the selected output power.

The crucible traverse rate was selected on the basis of previous work,[13] as it affects the volume of melt attained during processing and, consequently, the solidification process. In addition, The cooling rate is fundamentally affected by the melt/solid interface, which for these systems is estimated at approximately 10^5 K/m.[20] Crystal order is, however, controlled largely by the traverse rate, which in this study is purposely kept constant.

In order to remark the advantages posed by an optical line scan configuration[12] and, in view of the beam scan configuration, most commonly reported in the literature,[13] Figure 1b illustrates their differences with respect to directional solidification from a melt.

As may be deduced from Fig 1b, beam scanning may promote solidification of phases in a fan-like microstructure distribution,[21] with a resultant entanglement of grains grown within a radial-like directional orientation when they exhibit an appreciable degree of crystallinity. In contrast, line scanning configurations yield much more ordered microstructures with an observable degree of directionality.[9–12]
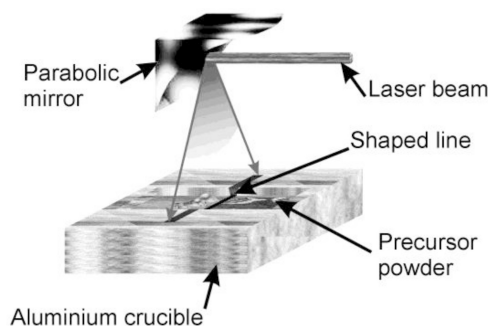
Transmission Electron Microscopy

The microstructure of the five samples (undoped and Fe_2O_3-doped TiO_2) was observed by transmission electron microscopy (TEM) and scanning TEM (STEM) on a JEOL JEM 3000F microscope. The microscope is equipped with an EDS INCA microanalysis suite and a Gatan Enfina EELS spectrometer. The characterization of the microstructure was mainly performed in TEM mode. EELS line scans were acquired in STEM mode with a beam diameter of aprox. 0.3 nm and a convergence semiangle of 12 mrad. The EELS spectra collection semiangle was 18 mrad. The elemental line profiles were extracted from the core loss edges by background substraction using a power law background and integrating over an energy window across the corresponding core loss edges.
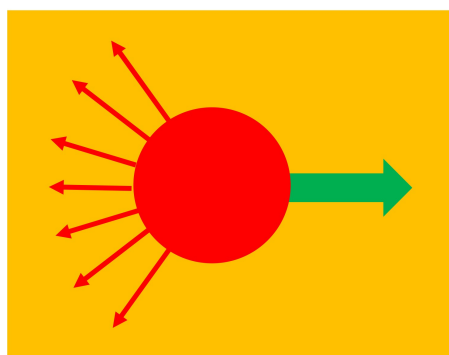
Results and Discussion

Optical Microscopy

Optical microscopy was used to observe the color and aspect of the products obtained, as well as to infer the degree of melting and the apparent level of homogeneity. The laser-treated pure titanium oxide product thus appears to have melted completely and exhibits a green-blue color. The latter is typically observed for TiO_2 when oxygen loss occurs at high temperatures.[22] The color of the TiO_2 + xFe_2O_3 mixtures varies from brown-red to black with increased iron oxide content. Representative photographs are shown in Figure 2 for samples with two distinct doping compositions, corresponding to x values of 0.03 (Figure 2a) and 0.01 (Figure 2b), respectively. For the sake of comparison, a photograph obtained from a pure TiO2 sample

Table 1. Composition of the powder mixtures subjected to study in this work.

x in (TiO_2 + xFe_2O_3)	% mol Fe_2O_3	$Fe_2Ti_{n-2}O_{2n-1}$ $n = (1/x) + 2$	Oxygen/Metal ratio $r = (2n-1)/n$
0.005	0.5	202	1.995
0.01	1	102	1.990
0.02	2	52	1.981
0.03	3	35	1.971

Beam Scan   Line Scan

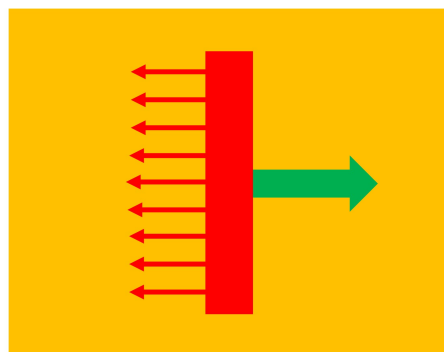**Figure 1.** a) Experimental apparatus used for Selective Laser Line Scan Synthesis in this study. It includes an IR emitting (l = 10.6 μm) CO2 laser, a parabolic mirror and a motorized linear motion stage, where a surface-treated Al crucible holds the solid powder mixture specified in Table 1. b) Difference between Laser Beam (left) and Line (right) scanning during melt processing of solid phases. In both cases, the red arrows indicate the direction of solidification, while the green arrows indicate the laser beam displacement. The circle (left) represents the melt form induced by a circular laser beam, while the thick vertical line (right) illustrates the ideal melt form generated by laser line scanning.
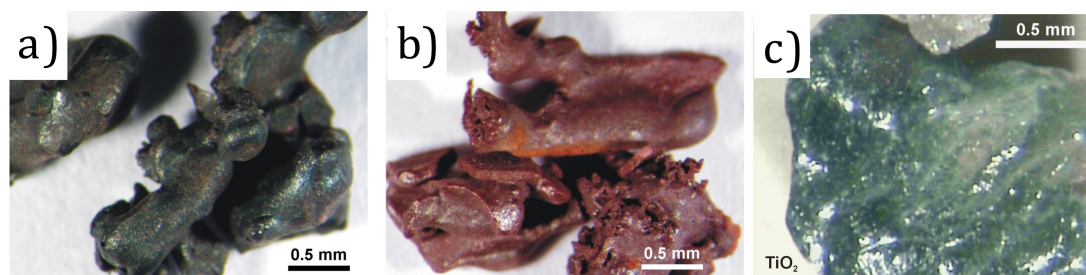

Figure 2. Photographs corresponding to CO_2 laser melting and solidification of $TiO_2 + xFe_2O_3$ mixture samples with x = 0.03 (a) and x = 0.01 (b) and x = 0.00 (c) as specified in Table I and following Laser Line Scan Synthesis (Figure 1).

after a similar treatment appears in Figure 2c. In principle, fine particles of hematite could be responsible for the color, suggesting that the application of this method to obtain useful pigments based on $TiO_2 + Fe_2O_3$ materials would need to be further investigated as a function of solidification rates and composition.

XRD Studies

XRD studies of the laser line scan synthesized samples are shown in Figure 3. These suggest that, upon laser treatment, rutile is identified in all cases as the main crystalline phase present in the product. This result is not surprising when considering the synthesis of Fe oxide doped Ti oxide, in view of previously published work.[3] Although the initial titanium oxide powder sample used as reactant contained basically rutile, the
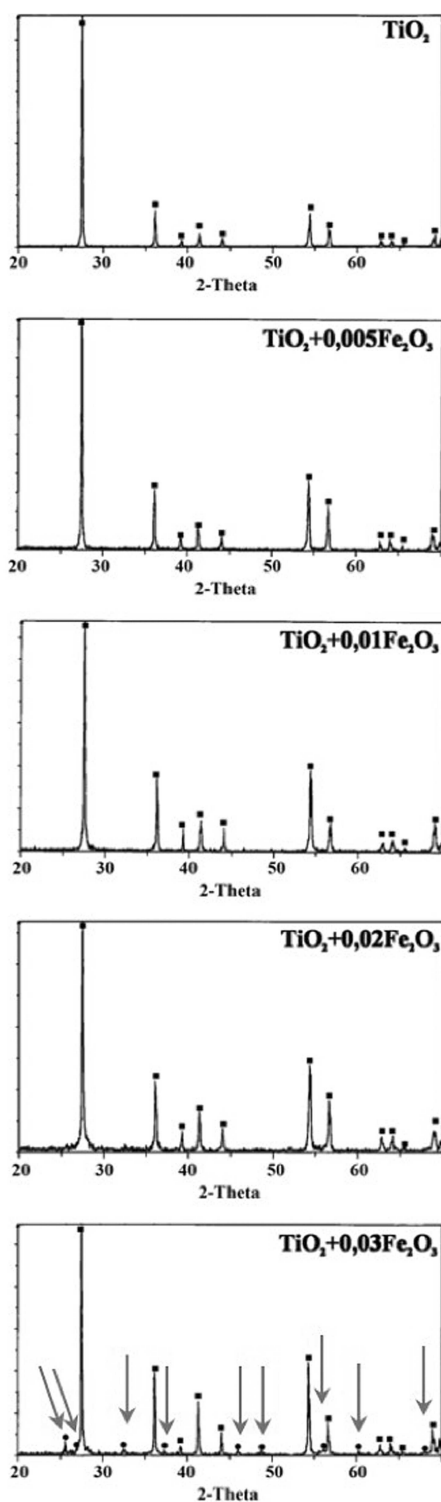
Figure 3. XRD patterns obtained on products prepared by Selective Laser Line Scan Synthesis. Main phases are identified as: ■- TiO_2 rutile, arrows and ● - Pseudobrookite Fe_2TiO_5.

TiO_2.[3] These results are thus expected for all of the doped samples studied.

Traces of the pseudobrookite phase were, however, clearly found in the sample with 0.03 mol% Fe_2O_3 content. The samples with lower iron oxide admixture exhibit diffraction lines corresponding only to the structure of the pure rutile phase, although the presence of pseudobrookite in the 0.02 mol% Fe_2O_3 sample cannot be ruled out, as its content may be below the detection level under the diffraction conditions imposed. There is no significant shift of diffraction lines when comparing samples with different iron oxide content. This suggests that, in principle, no other Fe oxides have been formed in detectable amounts during the laser synthesis process.

Furthermore, the pure Rutile phase sample, molten in the laser line and directionally solidified exhibits the XRD pattern shown in Figure 3a. Although the color of this sample is light blue-green, the x-ray diffraction pattern presents only the rutile phase with a = **4.5795 Å** and c = **2.952 Å**, which fits well to the rutile reference PDF#21-1276 (4.5933x2.9592). The samples with 0.5, 1 and 2 mol% of Fe_2O_3 doped TiO_2 only exhibit x-ray powder patterns with rutile type maxima (see Figure 3b, c, d). The formulation of these samples as mixed oxides would correspond to $Fe_2Ti_{200}O_{403}$ (O/M (FeTi) = 1.995), $Fe_2Ti_{100}O_{203}$ (O/M (FeTi) = 1.990), and $Fe_2Ti_{50}O_{103}$ (O/M (FeTi) = 1.981). The X-ray powder diffraction data suggest a good level of solubility of hematite (α-Fe_2O_3) in rutile. The cell parameters calculated from the X-ray data are presented in Table 2.

In the case of the sample with 3 mol% Fe_2O_3, i.e. $Fe_2Ti_{33}O_{69}$ (O/M = 1.971), the X-ray powder pattern is indexed as a mixture of two phases: (i) pseudobrookite Fe_2TiO_5, with parameters a = 9.7559 Å, b = 9.9923 Å and c = 3.7262 Å, and (ii) rutile type TiO_2 with the parameters displayed in Table 2.

TEM and EELS Investigations

The TEM/HRTEM observations confirm the presence of crystals with the same rutile basic structure, although their lattices contain areas with extended crystallographic shear plane (CSP)-type defects parallel to $(121)_r$, $(021)_r$ and $(132)_r$. Their number increases directly with increasing presence of iron oxide. A variety of extended defects was found, however, in all of the directionally solidified laser melted samples.

In the pure rutile samples, for example, multiple twinning type defects were most commonly found. These may be observed in Figure 4, where TEM micrographs obtained under

fast solidification rates applied did not seem to favor formation of Anatase upon rapid solidification from the melt, as suggested in previous studies.[23] In addition, the presence of Fe oxide has been suggested to strongly influence the formation of Rutile in

Table 2. Cell parameters calculated from XRD data for the Fe_2O_3 doped TiO_2 samples subjected to study.

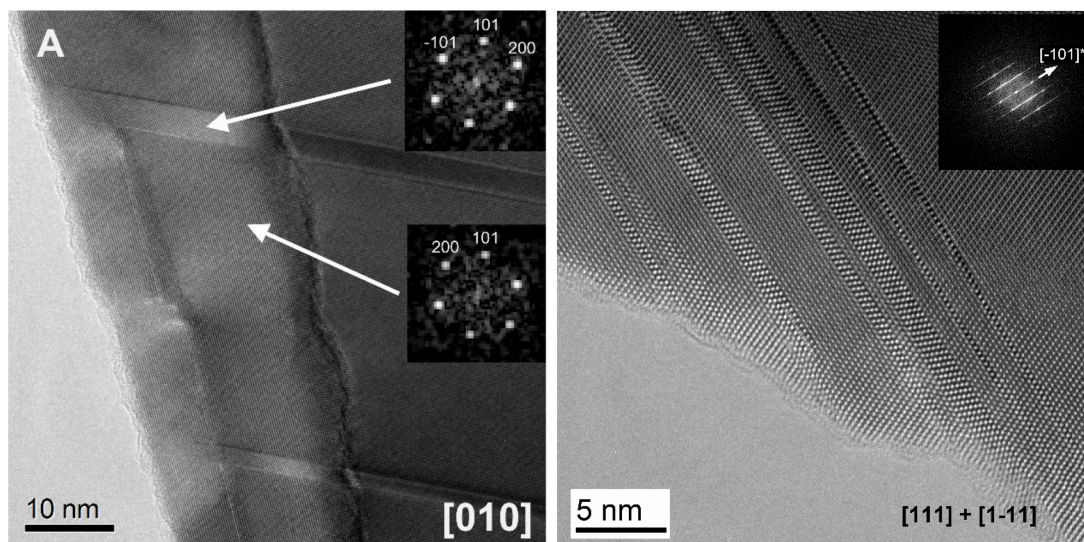| Doping amount, %mol of Fe_2O_3	Phase	a, Å	c, Å
0	Rutile	4.5795	2.9520
0.5	Rutile	4.5704	2.9658
1.0	Rutile	4.5696	2.9737
2.0	Rutile	4.5822	2.9640
3.0	Rutile	4.5822	2.9702

Figure 4. a) Low magnification TEM image of a crystal flake of the pure TiO_2 sample, where the particle is oriented along the $[010]_r$ zone axis of the rutile structure. Several extended defects were found in the laser processed sample. The insets show the power spectra of two crystalline domains in the TEM image with a twin orientation on $\{101\}_r$. b) TEM image of a different particle showing multiple twinning on a finer scale.

different magnification are shown. In particular, Figure 4a) corresponds to a low magnification TEM image of a pure TiO_2 sample crystal flake, oriented along the $[010]_r$ zone axis of the rutile structure. Several extended defects are observed in this laser processed sample. The insets show the power spectra of two crystalline domains with a twin orientation on $\{101\}_r$. On the other hand, Figure 4b) corresponds to a TEM image obtained on a different particle which exhibits multiple twinning on a finer scale.

A low magnification TEM image showing extended defects in the $TiO_2 + 0.005Fe_2O_3$ sample is given in Figure 5a). The arrows point to some faults aligned edge on, whereas arrowheads highlight defects inclined with regard to the electron beam. For this same sample, an enlarged TEM image is provided in Figure 5b). Here, the thin dark line features observed correspond to parallel isolated CSPs oriented along the edge, while the broader strip features correspond to CSPs with a slightly different orientation.
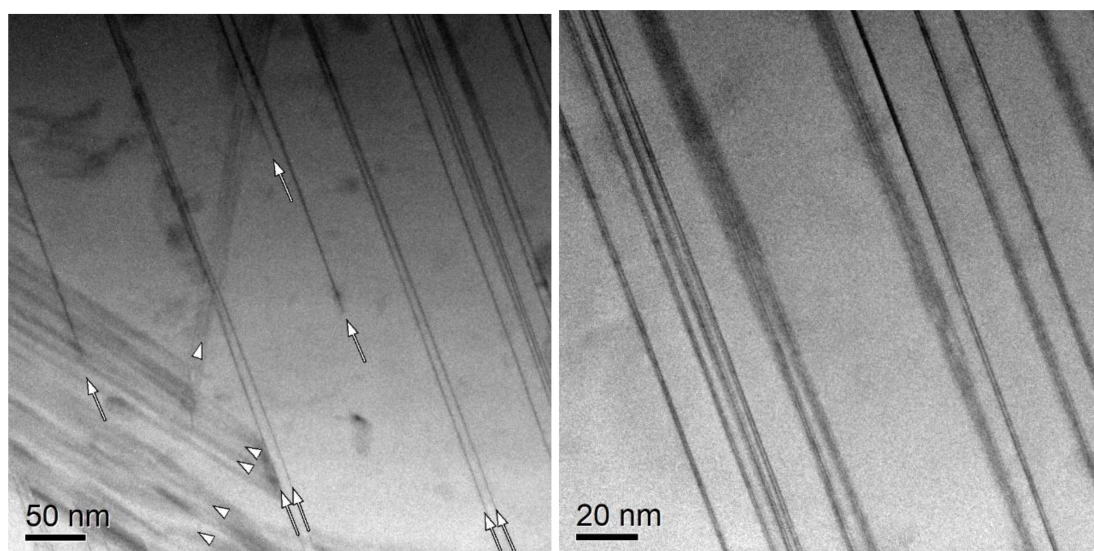

Figure 5. a) Low magnification TEM image showing extended defects in the sample with composition $TiO_2 + 0.005Fe_2O_3$. The arrows point to some faults aligned edge on, whereas arrowheads highlight defects inclined with regard to the electron beam. b) Enlarged TEM image where the thin dark lines are parallel isolated CSPs oriented edge on, sometimes running in pairs close together; the broader, more diffuse strips, correspond to CSPs with a slightly different orientation.

The effect of increased Fe_2O_3 doping is observed in Figure 6a), which provides a TEM micrograph taken on a thin edge of an iron doped rutile crystal of the $TiO_2 + 0.01Fe_2O_3$ sample. The image shows quasi ordered $\{121\}_r$ CSP's[5] in a twinned arrangement, i.e., along $(211)_r$ and $(-211)_r$ of rutile. The inset corresponds to the power spectra of a small defect-free area. Figure 6b) on the other hand, shows a TEM image of a multiple twinned particle taken along the $[1-11]_r$ zone axis, with the inset highlighting the power spectrum of a single twin domain.

Further doping effects are observed in Figure 7a), where a low magnification TEM image, taken on a crystal of the $TiO_2 + 0.02Fe_2O_3$ sample with a complex texture, is shown. The wavy contrast of the image is due to the presence of a high number of extended CSP type defects within the rutile matrix. Their orientation is close to $\{121\}_r$, although in some areas they swing towards a different crystallographic direction. In addition, Figure 7b) provides an enlarged TEM image showing CSPs running along a high $(hkl)_r$ index orientation. Splitting can be appreci-
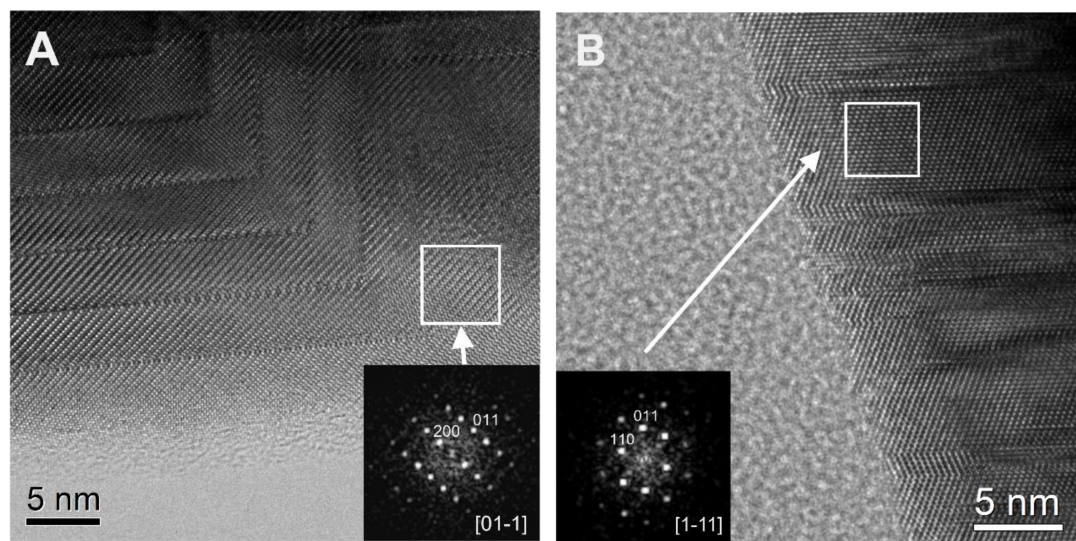

Figure 6. a) TEM micrograph taken on a thin edge of an iron doped rutile crystal of the $TiO_2 + 0.01Fe_2O_3$ sample. The image shows quasi ordered $\{121\}_r$ CSP's[5] in a twinned arrangement, i.e., along [211]* and [-211]* of rutile. The inset corresponds to the power spectrum of the small defect free area marked in the TEM image. b) TEM image of a multiple twinned particle taken along the $[1-11]_r$ zone axis, the inset shows the power spectrum from a single twin domain marked in the TEM image.
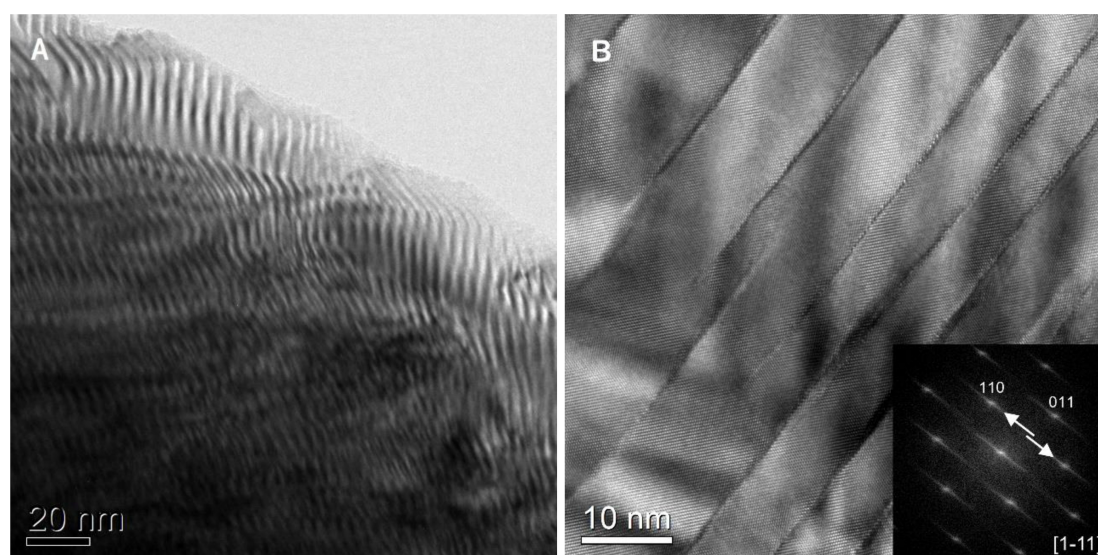

Figure 7. a) Low magnification TEM image taken on a crystal of the $TiO_2 + 0.02Fe_2O_3$ sample with a complex texture. The wavy contrast of the image is due to the presence of a high number of extended defects of the CSP's type in the rutile matrix, slightly misoriented with the electron beam; their orientation is close to $\{121\}_r$ but in some areas they swing to a different direction. b) Enlarged TEM image showing CSPs running along a high (hkl) index orientation. See the splitting in the diffuse streaks in the corresponding power spectrum.

ated in the diffuse streaks within the corresponding power spectrum in the inset.

A representative micrograph for the sample with the highest doping level is provided in Figure 8, which corresponds to a TEM image taken on a particle of the $TiO_2 + 0.03Fe_2O_3$ sample. The apparent zig-zag pattern observed in the image is a consequence of CSPs running along two equivalent $\{121\}_r$ directions of the rutile structure. The inset shows the power spectrum of the complete image.

Moreover, the TEM/HRTEM observations of the iron doped rutile samples also show crystals with the basic rutile structure, although their matrices contain areas with extended defects of the Crystallographic Shear Plane (CSP) type[16–19] (see Figures 5–8). In most cases, these defects are parallel to $\{121\}_r$, but they can also have orientations intermediate between $\{121\}_r$ and $\{132\}_r$. This is not surprising, in fact, because in pure rutile reduced samples, the CSPs orientation can change continuously (swinging) from $(121)_r$ to $(132)_r$.[19]

The present study of the laser processed iron doped rutile samples confirms that the number of extended defects increases with increasing levels of iron oxide doping. This seems to be consistent with the fact that, in Fe-doped Ti oxide samples, the iron is segregated on the CSP type extended defects, whereas the rutile basic structure matrix only contains titanium oxide doped with a very small amount of iron. This is in fact confirmed by EELS line scans acquired across isolated CSPs for an Fe-doped rutile crystal with $TiO_2 + 0.03Fe_2O_3$ composition (see Figure 9a). The corresponding core loss signals extracted for Fe, Ti and O (Figure 9b) show an increase of the iron concentration in the defects, accompanied by a reduction of the titanium and oxygen concentrations.

Crystals with the pseudobrookite structure type (Fe_2TiO_5)[24,25] with titanium excess were also found in the $TiO_2 + 0.03Fe_2O_3$ laser synthesized sample (see Figure 10a). This is consistent with substitution of Fe^{3+} by Ti^{3+} (reduction of Ti^{4+} during the laser treatment), or by reduction of Fe^{3+} to Fe^{2+} and substitution of Fe^{3+} by Ti^{4+}. This type of redox phenomena could be consistent with work previously reported in the literature,[26] as well as with laser induced melt processes where high temperatures are readily achieved.[22,27]

Figure 10b shows a [011] zone axis HRTEM image of one crystal with the pseudobrookite structure in the $TiO_2 + 0.03Fe_2O_3$ sample. Clusters or small coherent precipitates on the thin edge of the crystal are marked by arrows. These clusters could be formed during fast solidification from the laser melt, particularly if the solidification rate is not constant. This can be a problem associated with the interplay between surface tension within the melt and the interaction of the latter with the crucible or the already solidified material below the melt. Furthermore, it may also be related to the growth of new oxide affecting the expansion of radiation effects and the presence of higher laser-induced electric fields and associated hole diffusion along the irradiated surface.[27]
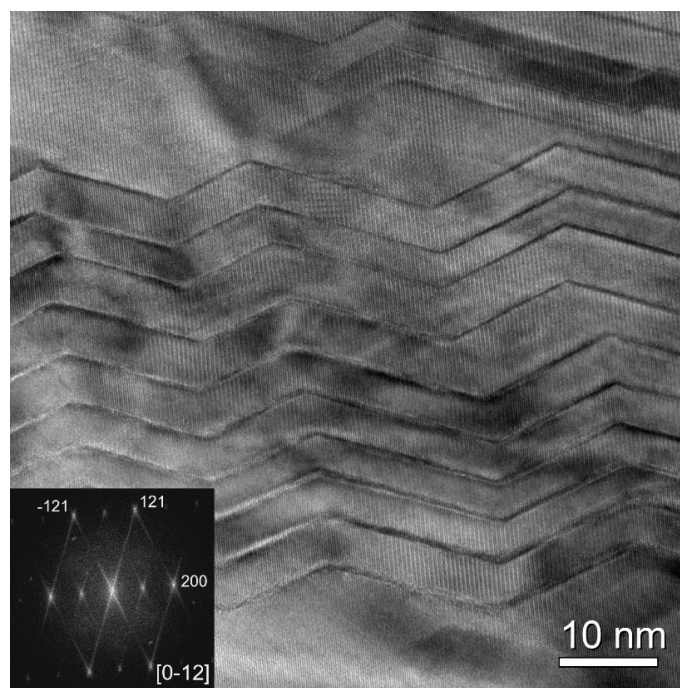

Figure 8. TEM image taken along the [0–12] zone axis on a particle of the $TiO_2 + 0.03Fe_2O_3$ sample, The apparent zig-zag pattern observed in the image is due to CSPs running along two equivalent $\{121\}_r$ directions of the rutile structure. The inset shows the corresponding power spectrum of the complete TEM image.
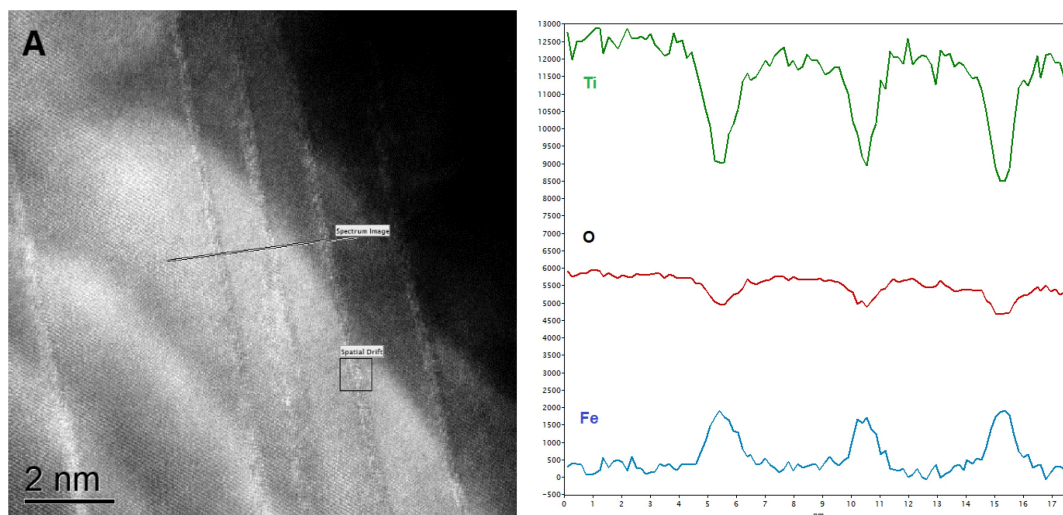
Figure 9. a) HAADF STEM image showing an EELS line scan acquired across three isolated CSPs found in an iron doped rutile crystal of the $TiO_2 + 0.03Fe_2O_3$ sample; b) Extracted core loss signals for $Fe-L_{3,2}$, $Ti-L_{3,2}$ and O-K.

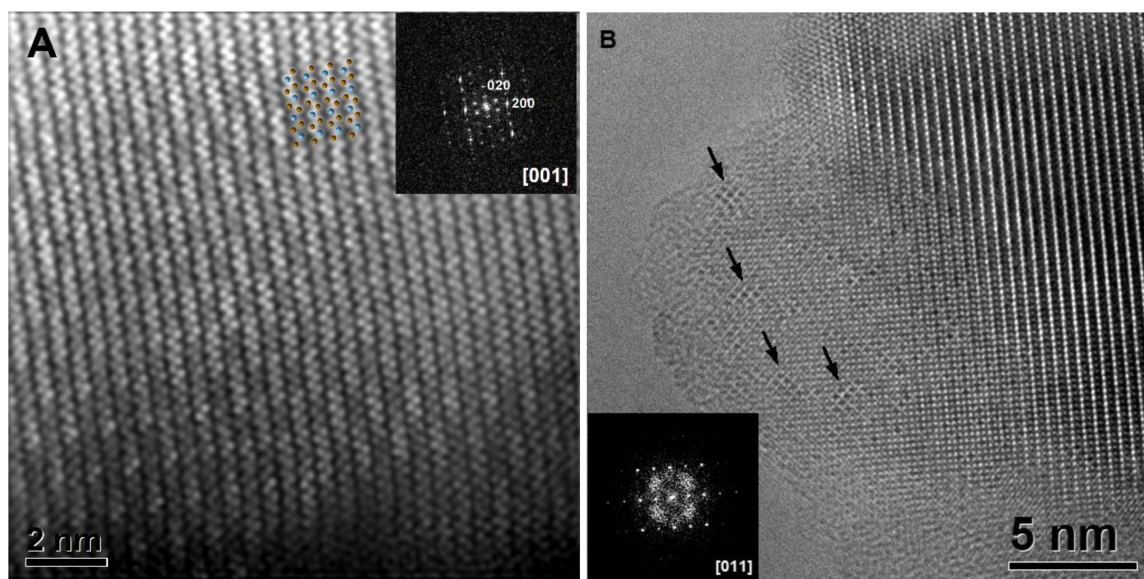**Figure 10.** a) Wiener filtered HAADF STEM image of a particle with pseudobrookite structure found in the sample with the composition $TiO_2 + 0.03Fe_2O_3$. A $^{[001]}$ projection of the pseudobrookite structure is overlayed on the image (the oxygen atoms have been removed for clarity). The inset shows the corresponding power spectrum with the diffraction spots indexed in the orthorhombic substructure. Notice the subtle modulation of the contrast in the image and the associated satellite reflections. b) HRTEM image of a particle with pseudobrookite structure taken along the $^{[011]}$ zone axis. Clusters or small coherent precipitates on the thin edge of the crystal are marked by arrows. These clusters could be formed during fast solidification from the laser melt.

Conclusions

A proof-of-principle for the rapid Selective Laser Line Scan Synthesis was demonstrated by applying a CO_2 laser emitting at 10.6 μm to TiO_2-Fe_2O_3 powder mixtures contained in an Al crucible. The synthesis process took place at temperatures approaching 2000 °C and at linear rates of 50 mm/min, which enable synthesis yields in the range of grams per minute.

The main phase formed during laser synthesis was a solid solution with a limited Fe content range. Iron doped rutile forms Crystallographic Shear Plane (CSP) type extended defects within the rutile lattice. These CSPs are the main type of defects found in the laser-synthesized materials herein reported, and their appearance may be linked to the fast solidification rates found in the Selective Laser Line Scan Synthesis procedure employed, as well as to laser irradiation effects. The HRTEM study shows that the amount of CSP extended defects found in

these samples increases with their iron oxide doping level. Elemental profiles of iron, titanium and oxygen were obtained across CSP's oriented along the edge via line scan EELS; the acquired line profiles show iron segregation in the CSP's extended defects. This fast and simple synthesis method opens new ways to attain solids under nonequilibrium conditions with the possibility of controlling solidification rates and thus their structural order and properties.

Conflict of Interest

The authors declare no conflict of interest.

Data Availability Statement

The data that support the findings of this study are available from the corresponding author upon reasonable request.

[1] F. Parrino, L. Palmisano, Titanium Dioxide (TiO_2) and Its Applications, in Metal Oxide Series, ISBN 978-0-12-819960-2, https://doi.org/10.1016/C2019-0-01050-3, Elsevier (2021).

[2] B. O. O'Regan, M. Grätzel, *Nature* **1991**, *353*, 737. http://doi.org/10.1038/353737a0.

[3] F. Gracia, J. P. Holgado, F. Yubero, A. R. González-Elipe, *Surf. Coat. Technol.* **2002**, *158*, 552–557. https://doi.org/10.1016/S0257-8972(02)00305-5.

[4] F. Gracia, J. P. Holgado, A. Caballero, A. R. González-Elipe, *J. Phys. Chem.* **2004**, *B108*, 17466–17476. https://doi.org/10.1021/jp0484938.

[5] Y. Ku, P-H Lin, H-C Wu, Y-C Liu, Y-H Tseng, H-Y Lee, *Aerosol Air Qual Res* **2017**, *17*, 2300–2309.https://doi.org/10.4209/aaqr.2017.03.0121.

[6] M. V. Tsodikov, O. V. Bukhtenko, O. G. Ellert, V. M. Shcherbakov, D. I. Kochubey, *J. Mater. Sci.* **1995**, *30*, 1087. https://doi.org/10.1007/BF01178450.

[7] V. Augugliaro, A. Lauricella, L. Rizzuti, M. Schiavello, A. Sclafani, *Int. J. Hydrogen Energy* **1982**, *7*, 845. https://doi.org/10.1016/0360-3199(82)90002-7.

[8] Escribano, P., J. B. Carda, E. Cordoncillo, Esmaltes y pigmentos cerámicos, Enciclopedia cerámica 1, Faenza Editrice Ibérica (2001). ISBN : 8487683193 9788487683190.

[9] A. Larrea, G. F. de la Fuente, R. I. Merino, V. M. Orera, *J. Eur. Ceram. Soc.* **2002**, *22*, 191–198. http://doi.org/10.1016/S0955-2219(01)00279-5.

[10] M. Mora, J. C. Diez, C. I. López-Gascón, E. Martínez, G. F. de la Fuente, *IEEE Trans. Appl. Supercond.* **2003**, *13*, 3188–3191. http://doi.org/10.1109/TASC.2003.812192.

[11] L. A. Angurel, J. C. Diez, G. F. de la Fuente, *Z. Anorg. Allg. Chem.* **2009**, *635*, 1767–1772. https://doi.org/10.1002/zaac.200900267.

[12] V. Lennikov, B. Özkurt, L. A. Angurel, A. Sotelo, B. Özçelik, G. F. de la Fuente, *J. Supercond. Novel Magn.* **2013**, *26*, 947–952. https://doi.org/10.1007/s10948-012-1934-1.

[13] R. Aroz, V. Lennikov, R. Cases, M. L. Sanjuan, G. F. de la Fuente, E. Muñoz, *J. Eur. Ceram. Soc.* **2012**, *32*, 4363–4369. https://doi.org/10.1016/j.eurceramsoc.2012.06.013.

[14] M. Jansen, *Angew. Chem. Int. Ed.* **2002**, *41*, 3746. https://doi.org/10.1002/1521-3773(200221018)41:20<3746::AID-ANIE3746>3.0.CO,2-2.

[15] J. C. Schön, M. Jansen, *Z. Kristallogr.* **2001**, *216*, 361. https://doi.org/10.1524/zkri.216.6.307.20339.

[16] L. A. Bursill, *J. Solid State Chem.* **1974**, *10*, 72. https://doi.org/10.1016/0022-4596(74)90012-7.

[17] L. A. Bursill, I. E. Grey, D. J. Lloyd, *J. Solid State Chem.* **1976**, *16*, 331. http://doi.org/10.1016/0022-4596(76)90049-9.

[18] L. A. Bursill, D. J. Netherway, I. E. Grey, *Nature* **1978**, *272*, 405. https://doi.org/10.1038/272405a0.

[19] B. G. Hyde, S. Andersson (1989) Inorganic Crystal Structures. J. Wiley & Sons, New York.

[20] G. F. de la Fuente, J. C. Diez, L. A. Angurel, J. I. Peña, A. Sotelo, R. Navarro, *Adv. Mater.* **1995**, *7*, 853–856.

[21] J. Khare, Kaul Rakesh, P. Ganesh, Harish Kumar, R. Jagdheesh, A. K. Nath, *J. Laser Appl.* **2007**, *1*, 1–7. https://doi.org/10.2351/1.2402522.

[22] J. M. Knaup, J. Marx, T. Frauenheim, *Phys. Status Solidi RRL* **2014**, *8*, 549–553. https://doi.org/10.1002/pssr.201409042.

[23] Y. Li, T. Ishigaki, *J. Cryst. Growth* **2002**, *242*, 511–516. DOI:10.1016/S0022-0248(02)01438-0.

[24] L. Pauling, *Z. Kristallogr.* **1930**, *73*, 97–112. https://doi.org/10.1524/zkri.1930.73.1.97.

[25] M. Shiojiri, S. Sekimoto, T. Maeda, Y. Ikeda, K. Iwauchi, *Phys. Stat. Sol. A* **1984**, *84*, 55–64. https://doi.org/10.1002/pssa.2210840107.

[26] J. Liu, C. Cao, X. Liu, L. Zheng, X. Yu, Q. Zhang, L. Gu, R. Qi, W. Song, *Angew. Chem. Int. Ed.* **2021**, *60*, 15248–15253. https://doi.org/10.1002/anie.202102647.

[27] K. Leitner, J. W. Schultze, *Ber. Bunsenges. Phys. Chem.* **1988**, *92*, 181–187. DOI:10.1002/bbpc.198800040.